Supplementary Figures

Supplementary Figure 1

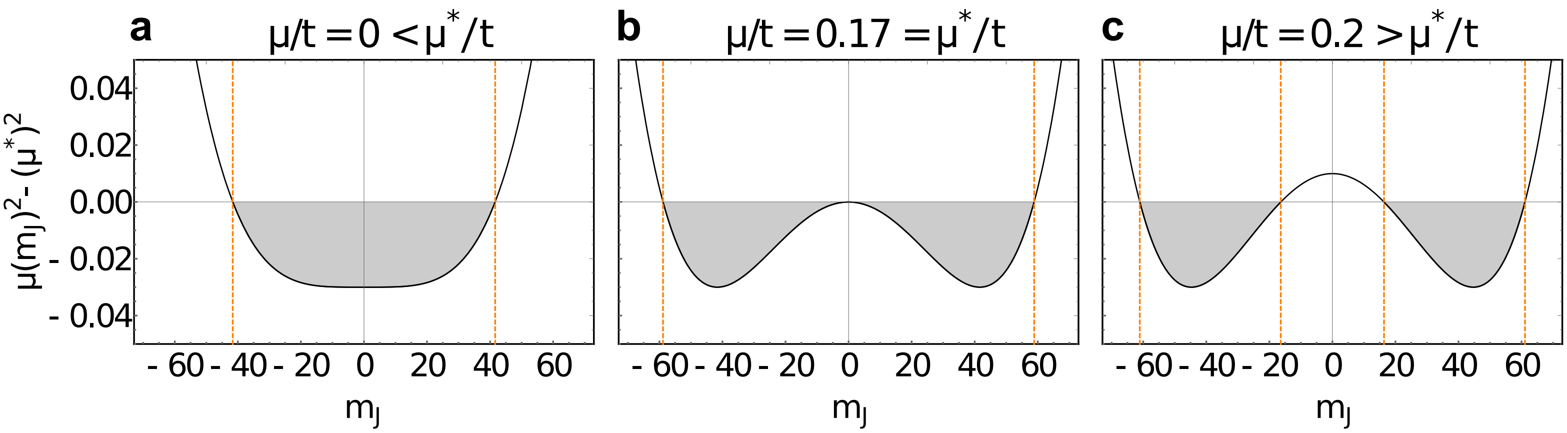

Supplementary Figure 1. **Influence of the chemical potential on the topological properties of the wire model.** The function $\mu\,(m_{\mathrm{J}})^2 - (\mu^*)^2$ for different values of the chemical potential μ, in a skyrmion of radius $R_{\mathrm{sk}}/a = 100$ and azimuthal winding number $q = 2$ with parameters $\Delta_0/t = 0.1$, $J/t = 0.2$. For these parameters $\mu^*/t = \sqrt{J^2 - \Delta_0^2} = 0.17(32)$. **a** $\mu/t = 0 < \mu^*/t$, **b** $\mu/t = \mu^*/t$ and **c** $\mu/t = 0.2 > \mu^*/t$. The gray areas show the topologically non-trivial momentum ranges while the vertical dashed orange lines mark the gap-closing momenta.

Supplementary Figure 2

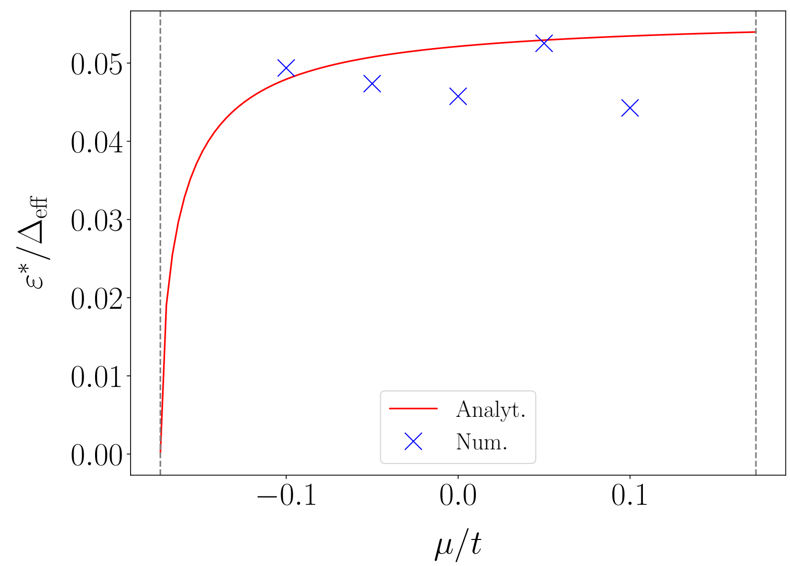

Supplementary Figure 2. **Near-flatness of the CMEM**. Ratio between the maximal energy attained by the CMEM states and the effective gap is plotted versus the chemical potential. The analytical estimate (red line) is given by Supplementary Equation 3 where we have chosen the prefactor of order unity to be $c \equiv 0.44$ (see text), while the numerical data (blue crosses) is obtained from the radial tight-binding skyrmion model. The parameters are $R_{\rm sk}/a = 1001$, $p = 10$, $q = 2$, $\Delta_0/t = 0.1$, $J/t = 0.2$. The vertical dashed gray lines mark the $|\mu| = \mu^*$ points.

Supplementary Figure 3

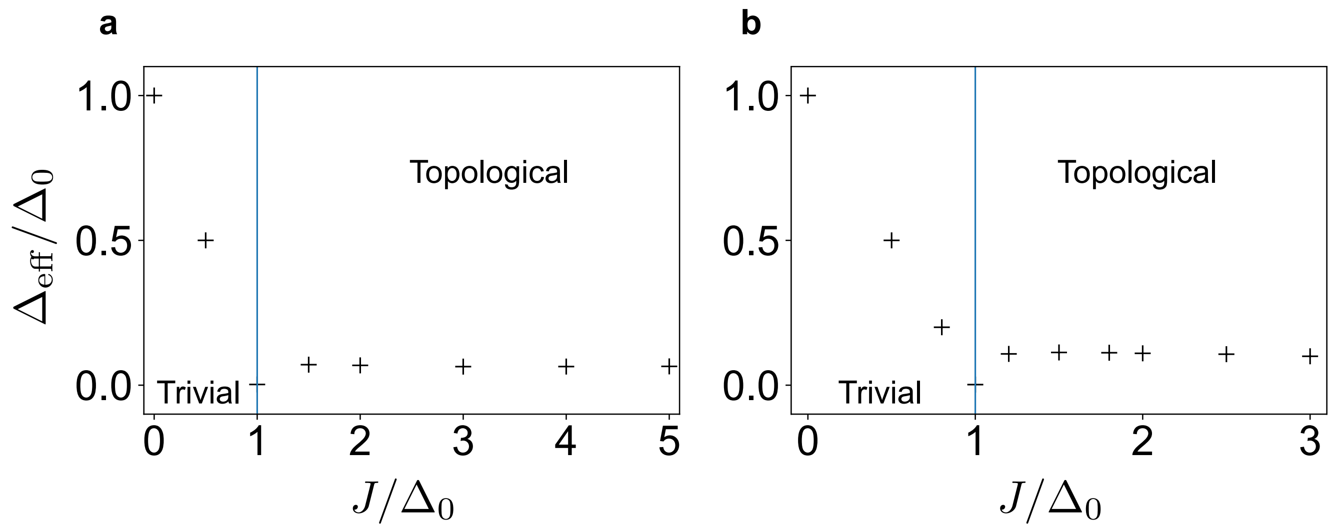

Supplementary Figure 3. **Comparing phase diagrams of the skyrmion model on disk and the model on cylinder.** Effective gap for $\mu/t = 0$ as a function of the exchange coupling J with $\Delta_0/t = 0.1$ in the radial tight-binding setup. **a** Skyrmion model on the disk geometry with $p = 10$ and $R_{\rm sk}/a = 1000$. **b** The mapped model on the cylinder with aspect ratio 1 and $R_{\rm sk}/a = 500$. In both **a** and **b**, the vertical blue line indicates the theoretical gap-closing point $J = \sqrt{\Delta_0^2 + \mu^2}$.

Supplementary Figure 4

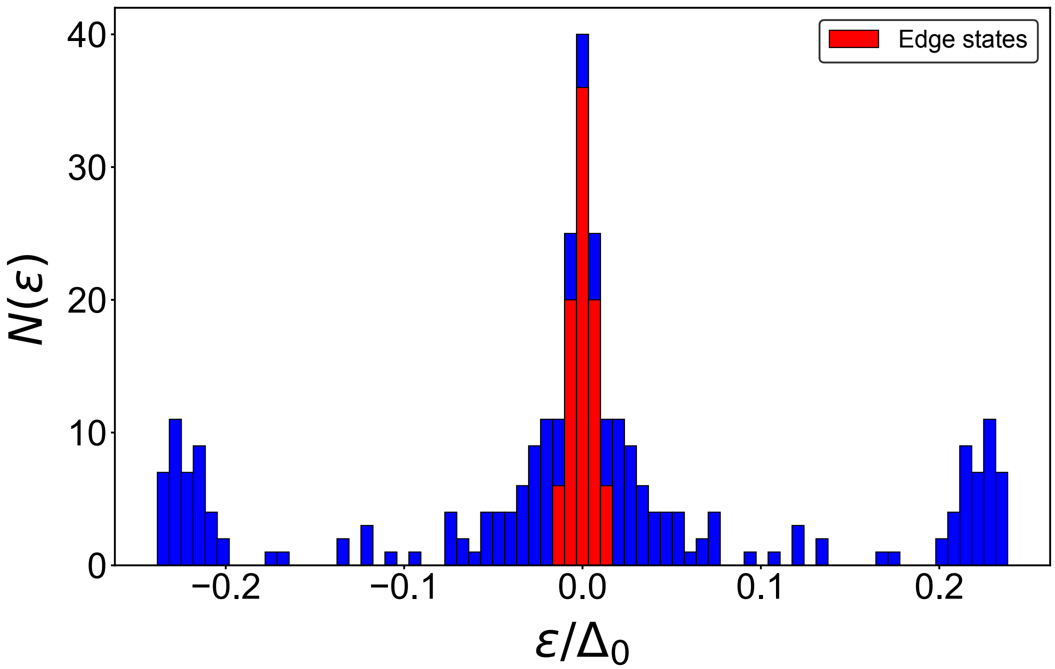

Supplementary Figure 4. **Counting the number of edge states.** Density of states at low energies for $p = 9$ and $q = 1$ circular skyrmion with $\lambda/a = 16$. The other parameters are $\mu/t = 0$, $\Delta_0/t = 0.1$, $J/t = 0.2$. The blue histogram represents the 300 lowest energy states, while the red histogram counts only the edge states among them (see definition in text, the selection criterion uses width $l = 3a$ which yields $l/\lambda \approx 0.19$). In this case there are 88 edge states. The coherence peaks in the density of states are clearly seen around $|\varepsilon/\Delta_0| \approx 0.2$. The result is consistent with an edge mode that very weakly disperses around zero energy. Other in-gap states, located in the bulk of the skyrmion, are attributed to impurity states (see main text).

Supplementary Figure 5

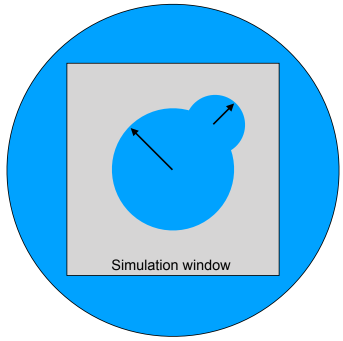

Supplementary Figure 5. **Defining geometries 2 and 3.** The largest blue disk (extending to outmost circle) represents a temporary large skyrmion texture. We define a texture with geometry 2 or 3 by setting the exchange $J = 0$ outside the inner blue region. The gray square shows the entire system kept in the calculation. The black arrows indicate the tunable radii, $r = R$ for geometry 2 and $r = R/2$ for geometry 3, where R is the radius of the central circle.

Supplementary Figure 6

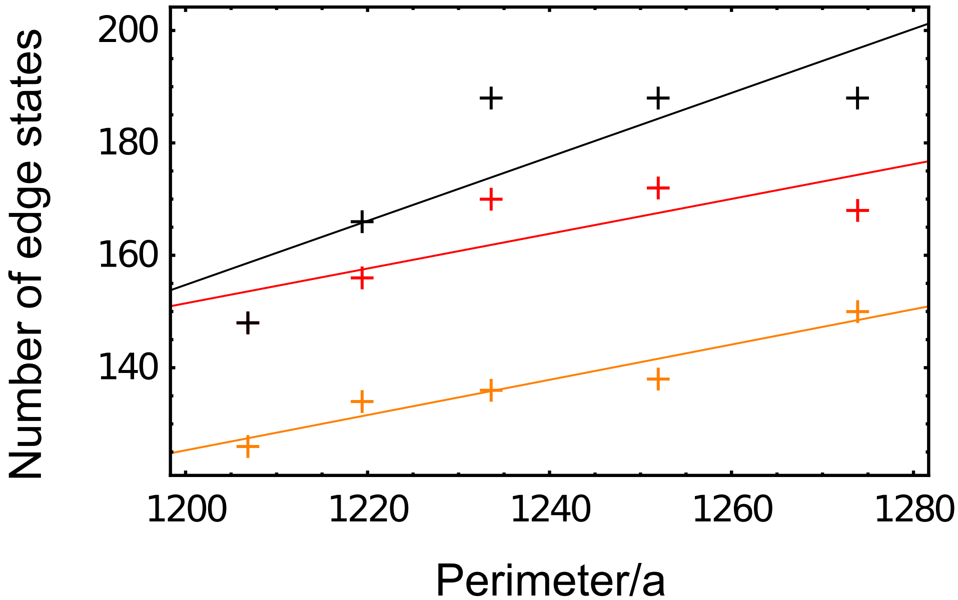

Supplementary Figure 6. **Counting the edge states in elliptical geometry**. Result of the counting of the edge states as a function of the perimeter in elliptical geometries for 3 different edge state selection criteria $l/\lambda = 0.25$ (orange), 0.33 (red) and 0.42 (black). Solid lines represent the best linear fit. The perimeter is varied by changing the aspect ratio of the ellipse while keeping its surface area fixed. The estimated slopes are $0.313\,a^{-1}$, $0.310\,a^{-1}$ and $0.569\,a^{-1}$, respectively.

Supplementary Figure 7

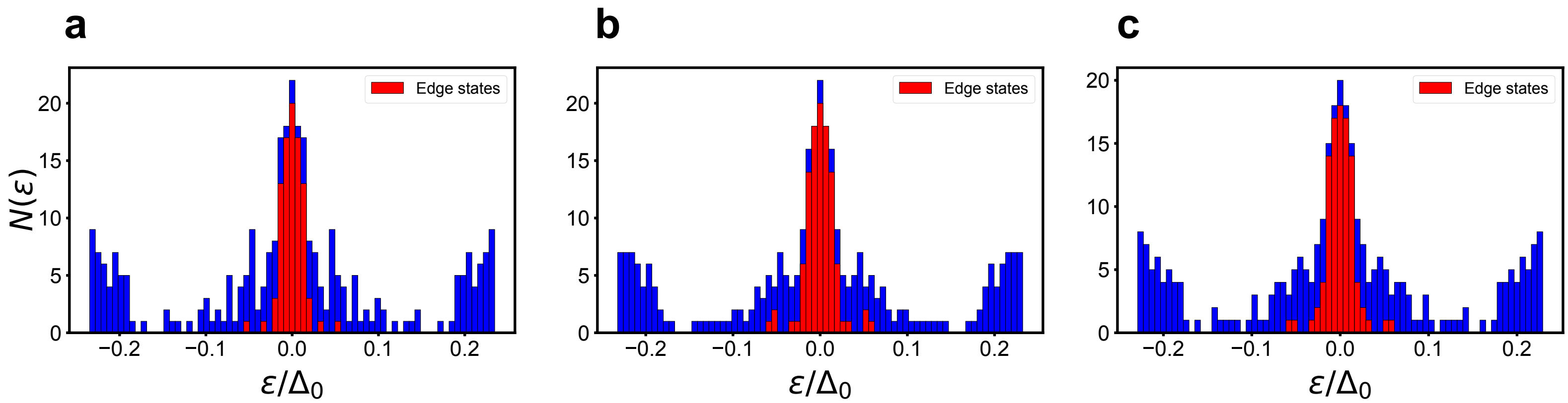

Supplementary Figure 7. **Robustness of the CMEM to scalar disorder in the 2D tight-binding model**. Starting from the same parameters as in Supplementary Figure 5 except that $q = 2$. We implement uncorrelated scalar disorder by randomly varying the on-site energy (see text). The variations are drawn from a normal distribution of mean μ and standard deviation $\sigma_\mu/\Delta_0 = 0.2$, 0.5, 0.7 for **a**, **b** and **c**, respectively.

Supplementary Figure 8

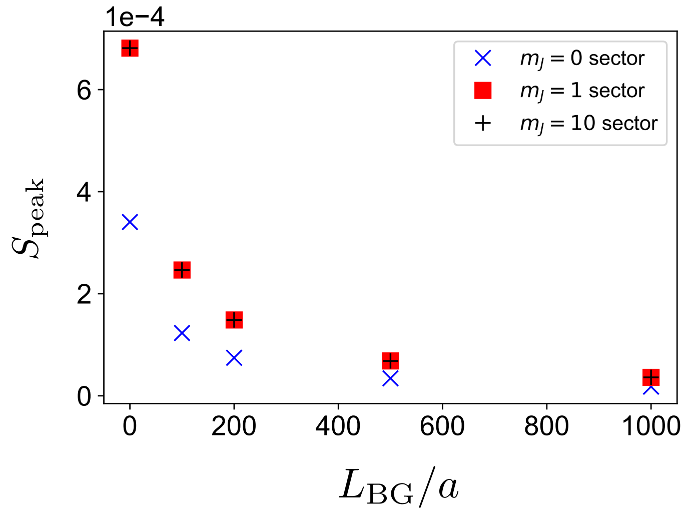

Supplementary Figure 8. **Delocalization of the edge states in a ferromagnetic background.** Scaling of the spectral weight $S_{\rm peak}$ under the peak of edge states as function of the background size L_{BG} for $L_{BG}/a \in \{0, 100, 500, 1000\}$ for $W_{\rm peak}/a \approx 200$ (from 800 to 1000) in the angular momentum sectors $m_{\rm J} = 0$, $m_{\rm J} = 1$ and $m_{\rm J} = 10$. The delocalization phenomenon holds in all sectors with the same decay length. The parameters used for the computation are $p = 10$, $R_{\rm sk}/a = 1000$, $\Delta_0/t = 0.1$, $\mu/t = 0$ and $J/t = 0.2$.

Supplementary Figure 9

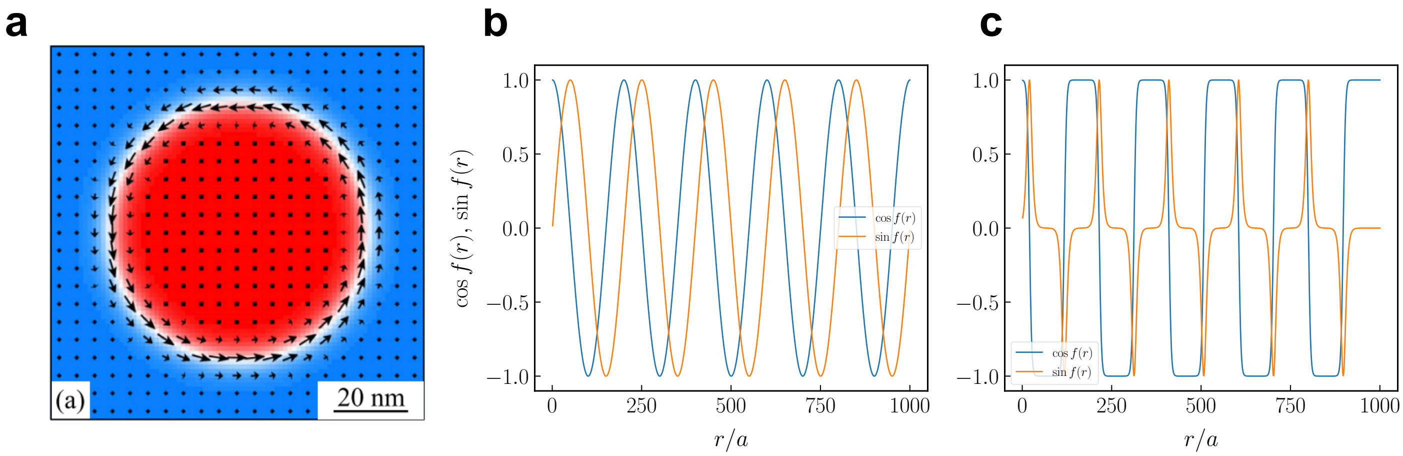

Supplementary Figure 9. **a** Real-space profile of a bubble. The arrows represent the in-plane components of the magnetization (n_x, n_y) while the color indicates the z component of the magnetization from -1 (red) to $+1$ (blue). Reprinted figure with permission from I. Makhfudz, B. Krüger and O. Tchernyshyov, *Physical Review Letters* **109**, 217201 (2012). Copyright (2012) by the American Physical Society. Our model of $p = 10$ **b** skyrmion and **c** bubble profiles. For the bubble the width of a domain wall is $w/a = 5$ (see Supplementary Equation 8).

Supplementary Figure 10

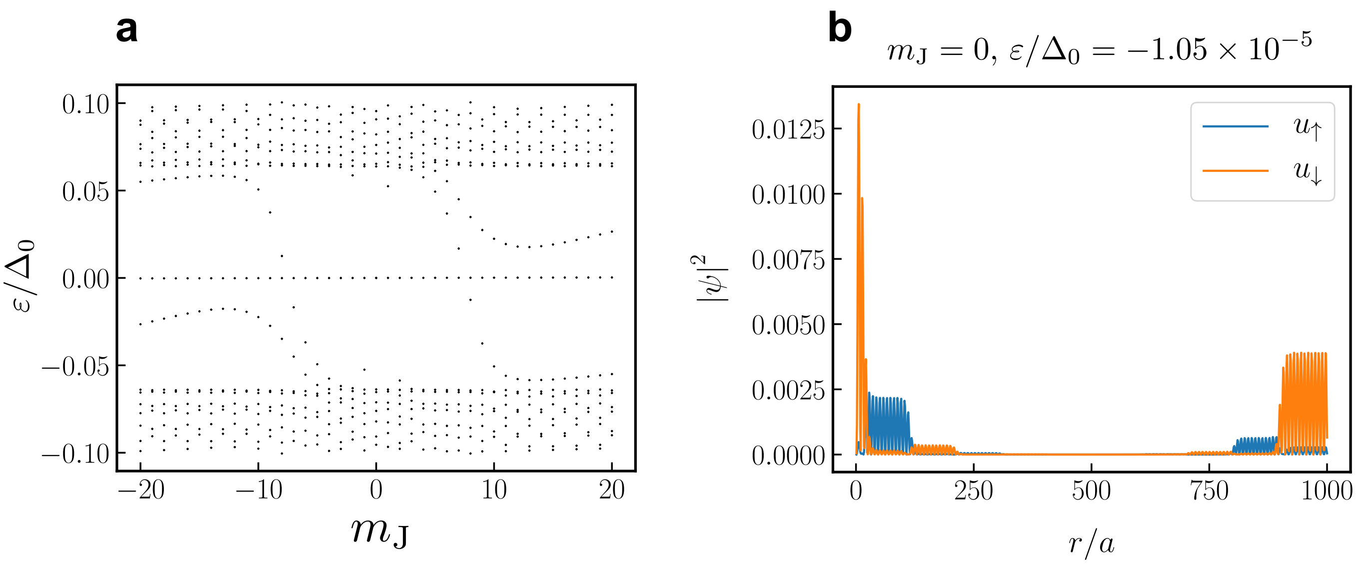

Supplementary Figure 10. Numerical diagonalization results for the parameters $p = 10$, $L = 1000$, $q = 2$, $J/t = 0.2$, $\Delta_0/t = 0.1$, $\mu/t = 0$ and a DW width $w/a = 5$. **a** Spectrum. **b** Density of one of the Majorana zero-modes.

Supplementary Notes

Supplementary Note 1 Topological transitions in the wire model

The wire Hamiltonian $\mathcal{H}^{\mathrm{wire}}_{m_\mathrm{J}}(r)$ (see Eq. (3) in the main text) corresponding to angular momentum sector m_J is in a topological phase when $\mu\left(m_\mathrm{J}\right)^2 - \left(\mu^*\right)^2 < 0$, where we introduced the quantity $\mu^* = \sqrt{J^2 - \Delta_0^2} > 0$. This leads to two cases. Firstly, Eq. (6) of the main text is only valid in the case $|\mu| < \mu^*$, and gives the two solutions presented there. Secondly, if $\mu > \mu^*$, solving for the gap-closing momenta yields four solutions $\pm\left|m^*_{\mathrm{J},\pm}\right|$, of the form

$$\left|m^*_{J,\pm}\right| \approx R_{\mathrm{sk}}\sqrt{\left(\mu \pm \sqrt{J^2 - \Delta_0^2}\right)} + \mathcal{O}\left(1\right). \tag{1}$$

Supplementary Figure 1 shows the different profiles of $\mu\left(m_\mathrm{J}\right)^2 - \left(\mu^*\right)^2$ depending on the ratio of μ and μ^*, where $\mu\left(m_\mathrm{J}\right) \equiv \mu - \left(m_\mathrm{J}^2 + \frac{q^2}{4}\right) / \left(2mR_{\mathrm{sk}}^2\right)$. Supplementary Figure 1c shows that in the second case discussed above (not presented in the main text), the momentum range $m_\mathrm{J} \in \left[-m^*_{\mathrm{J},-}, m^*_{\mathrm{J},-}\right]$ is topologically trivial while the ranges $m_\mathrm{J} \in \left[m^*_{\mathrm{J},-}, m^*_{\mathrm{J},+}\right]$ and $m_\mathrm{J} \in \left[-m^*_{\mathrm{J},+}, -m^*_{\mathrm{J},-}\right]$ are non-trivial as denoted by the gray filling of the curve. Consequently, in this regime of $\mu > \mu^*$ there is no Majorana zero-mode in the core of the skyrmion even if the azimuthal winding number q is even. The case $\mu < -\mu^*$ corresponds to the case of a fully topologically trivial system. These considerations were confirmed numerically in the radial tight-binding setup of the skyrmion model.

Supplementary Note 2 Velocity of the chiral Majorana edge mode

Treating $\mathcal{H}^{\mathrm{slope}}_{m_\mathrm{J}}(r)$ in Eq. (4) in the main text as a first order perturbation to the Majorana flat band (MFB) of the $q = 0$ model, we can estimate the upper limit on the energy ε^* that the CMEM reaches, which occurs at the maximal m_J of the CMEM, i.e. , $\varepsilon^* \equiv |\varepsilon^{\mathrm{edgestate}}(|m^*_\mathrm{J}*|)|$. This reads

$$\varepsilon^* = c\frac{q\, m^*_\mathrm{J}}{2mR_{\mathrm{sk}}^2} \tag{2}$$

where m^*_J is given by Eq. (6) in the main text, assuming the case $|\mu| < \mu^*$. We have also assumed $\langle\tau_z\sigma_z r^{-2}\rangle_{\mathrm{MFBstate}} = cR_{\mathrm{sk}}^{-2}$, taking into account that the edge states are very localized around R_{sk} for the relevant range of model parameters, and expecting that c is a constant of order unity.

The effective p-wave gap $\Delta_{\rm eff}$ being estimated by Eq. (9) in the main text, we obtain for the ratio between the maximal CMEM energy and the effective gap:

$$\frac{\varepsilon^*}{\Delta_{\rm eff}} = c\frac{q}{p}\frac{J}{\pi\Delta_0}\sqrt{\frac{\mu+\sqrt{J^2-\Delta_0^2}}{J+\mu}}, \tag{3}$$

where all energies are in units of the bandwidth t. We next compare this estimate to the numerical results in the radial tight-binding skyrmion model, see Supplementary Figure 2. First, we have calculated numerically the expectation value $\langle\sigma_z\tau_z\rangle_{\rm MFBstate}$ and indeed found typical values ≈ 0.44 of order unity. Supplementary Figure 2 shows a good agreement between our numerics and our analytical estimate for $c \equiv 0.44$. Due to the large size of the skyrmion used here to minimize finite-size effects, the ratio Supplementary Equation 3 is of order 5%. From the computation on smaller skyrmions and by varying parameters J, μ, we find that this value can be increased to at most $\approx 10\%$ and the CMEM therefore universally appears almost flat. In fact, our analytical estimate confirms that the near-flatness of the CMEM cannot significantly change by varying the parameters J, Δ_0 in their respective ranges under consideration (see Discussion).

Supplementary Note 3 Phase diagrams of the skyrmion model and the cylinder model

To support the use of our mapping from the disk to the cylinder, we here plot the two phase diagrams at a fixed value of the chemical potential $\mu/t = 0$. To do so, we tune the exchange coupling J and measure the effective gap, i.e. the gap in the $m_{\mathrm{J}} = 0$ sector. Supplementary Figure 3 clearly shows that the effective gap behaves the same way in both models, including the topological phase transition at the analytically predicted value $J = \sqrt{\Delta_0^2 + \mu^2}$. Moreover, the agreement in the topological regime is quantitative, while the small discrepancy can be accounted for by the fact that in the cylinder model we neglected the small chemical potential renormalization and the boundary term, Eq. (5) in the main text.

Supplementary Note 4 Different edge geometries: counting the states in the chiral Majorana edge mode

In this section we define the different geometries mentioned in the main text, as well as our technique for counting the edge states.

Counting the number of edge states of a circular skyrmion

We firstly investigate the original skyrmion texture that, dubbed "geometry 1". The circular edge of the original skyrmion texture ("geometry 1") is close to perfectly rotationally symmetric on the 2D lattice (except for the breaking of the spatial rotation symmetry down to the square lattice's discrete one). An eigenstate of the 2D tight-binding model is defined as an edge state if the maximum of its wavefunction lies in a certain corona of width $2l$ around the edge of the skyrmion at $r = R_{\mathrm{sk}}$. The position R_{max} of the maximum of the wavefunction is found using the angularly-averaged wavefunction. Precisely, a state is an edge state if $|R_{\mathrm{sk}} - R_{\mathrm{max}}| \leq l$. We will comment on the chosen values for l below. Based on this definition, the count of edge states for the circular skyrmion is presented in Supplementary Figure 4, where the cut-off l is 3 lattice sites so that $l/\lambda \approx 0.19$, given the skyrmion's value $\lambda/a = 16$.

Defining the geometries and edge state counting

Geometries 2 and 3 are obtained by defining a skyrmion in a large simulation window, and then defining the desired texture's edge by setting the exchange J to zero outside the edge curve, as shown in Supplementary Figure 5. The shape of the edge curve is defined as the outside perimeter of two overlapping disks. The second disk, of radius r is positioned so that its center lies on the perimeter of the first disk, which has radius R (Supplementary Figure 4). The exact perimeter of the resulting texture's edge (i.e. the outside perimeter of the overlapping disks), $P\left(\frac{r}{R}\right)$, reads

$$\frac{P\left(\frac{r}{R}\right)}{2\pi R} = 1 + \frac{r}{R} - \frac{1}{\pi}\arccos\left(1 - \frac{r^2}{2R^2}\right) - \frac{1}{\pi}\frac{r}{R}\arcsin\left(\sqrt{1 - \frac{r^2}{4R^2}}\right). \tag{4}$$

Alongside geometry 1, defined by a single circular edge of radius R_{sk} (i.e. the original skyrmion), the other two geometries presented in the main text are defined by disk radii $r = R$ (geometry 2) and $r = R/2$ (geometry 3). For comparisons, we set $R \equiv R_{\text{sk}}$.

In the case of non-circular edge shape, we straightforwardly generalize the edge state counting . Note that our geometries 2 and 3 are formed by adding an outward bulge to the circular edge of geometry 1. Therefore for simplicity we define as an edge state any state that satisfies $R_{\text{max}} \geq R_{\text{sk}} - l$. This criterion is less precise and may slightly overestimate the number of edge states. For simplicity we examine only the eigenstates whose energy is below $\Delta_{\text{eff}}/4$, recalling that the highest edge state energy is expected to be $\varepsilon^* \approx \Delta_{\text{eff}}/10$. In all studied cases the energy cutoff is $\approx 0.05\Delta_0$.

In all geometries presented here (1, 2 and 3), the variation of the perimeter was achieved by changing the overall spatial scale while keeping the number of sites per spin-flip the same.

Elliptic geometry

The elliptic geometry is defined simply by replacing the two-disk construction of Supplementary Figure 5 by a single ellipse at the center. We use the perimeter $P(a, b)$ of an ellipse of semi-major axis a and semi-minor axis b given as

$$P(a, b) = 4aE\left(\sqrt{1 - \frac{b^2}{a^2}}\right), \tag{5}$$

where $E(m)$ is the complete elliptic integral of the second kind defined as

$$E(m) = \int_0^{\frac{\pi}{2}} \sqrt{1 - m^2 \sin^2\theta}\, d\theta = \int_0^1 \frac{\sqrt{1 - m^2 t^2}}{\sqrt{1 - t^2}} dt. \tag{6}$$

The selection criterion for edge states is a simple generalization of the circular case (geometry 1) since the location of points on the edge of the ellipse is simply defined in cartesian coordinates. The perimeter is increased by changing the aspect ratio of the ellipse while keeping its surface area constant, starting from $p = 16$, $q = 2$ and $\lambda/a = 12$. The results and linear fits for different edge state selection criteria $l/a = 3$, 4, 5 ($l/\lambda = 0.25$, 0.33, 0.42) are shown in Supplementary Figure 6.

The fit results are:

- $l/\lambda = 0.25$: $0.31(36) \pm 0.05(35)\, a^{-1}$

- $l/\lambda = 0.33$: $0.30(95) \pm 0.13(74)\, a^{-1}$
- $l/\lambda = 0.42$: $0.56(93) \pm 0.21(87)\, a^{-1}$.

The data is clearly more noisy than in the case of other geometries, and the fit slopes deviate from the results of the main text (even within error bars, see Fig. 3 in the main text). We ascribe the discrepancy to the varying curvature of the texture's edge that causes hybridization between the wavefunctions on the edge. Note that in geometries 2 and 3 the edge has a non-constant curvature only at isolated points (where two circles meet).

Supplementary Note 5 Stability to disorder in the 2D tight-binding model

The robustness of the chiral Majorana edge mode is further confirmed by an analysis of the effect of scalar disorder in the 2D tight-binding model. The disorder is a random, spatially uncorrelated variation of the on-site energy applied throughout the system: $\mu \to \mu + \delta\mu$ where $\delta\mu$ is distributed according to a normal law of mean 0 and standard deviation σ_μ.

In Supplementary Figure 7 we show the results for varying disorder strengths $\sigma_\mu/\Delta_0 = 0.2, 0.5, 0.7$ in the case of the $p = 9$ and $\lambda/a = 16$ skyrmion.

An example of a clean system's density of states is shown in Supplementary Figure 4. While for the particular clean system whose parameters exactly correspond to the disordered systems here, there are 90 edge states in the energy range $\pm 0.05\,\Delta_0$. The density of states of the disordered systems, including the count of edge states in the energy range $\pm 0.05\,\Delta_0$, namely, 90, 106, and 98 states

for Supplementary Figure 7a, b and c, respectively, confirm that the edge mode is stable to relatively high disorder strengths.

Supplementary Note 6 Delocalization of the edge states in a magnetic background

Yang et al (Supplementary Reference 1) predict that if a constant magnetic background is added outside the skyrmion then the edge states delocalize from the edge into this background. The reason is simply that the superconductor is gapless in the background region. This is readily verified numerically in the radial tight-binding model of the skyrmion, as shown in Supplementary Figure 8 where we plot the spectral weight of the peak of the edge state as the size of the background region is increased. Defining the wavefunction as $(u_\uparrow(r), u_\downarrow(r), v_\downarrow(r), v_\uparrow(r))$, we compute the spectral weight S_{peak} of the state's peak through the $u_\uparrow$ component, as

$$S_{\text{peak}} \approx \frac{1}{W_{\text{peak}}} \sum_{j \in \text{peak}} |u_\uparrow(j)|^2 \tag{7}$$

where W_{peak} is the estimated width (i.e. length in radial direction) of the peak of the edge state. We plot the results for S_{peak} as a function of the background region size (i.e. length in radial direction) in Supplementary Figure 8.

Supplementary Note 7 Magnetic bubbles

For our model the most important spatial feature of bubbles is that they are essentially annulus-shaped domains of uniform polarization separated by ring-shaped domain walls Supplementary Reference 2–5, see Supplementary Figure 9a. We therefore contrast such a straightforward model of a bubble with our model of the skyrmion in Supplementary Figure 9b,c. In Supplementary Figure 9b the skyrmion shows smooth oscillation between out-of-plane (blue line is z-component) and in-plane magnetization (orange line). In contrast, the bubble, Supplementary Figure 9c, has magnetization roughly out-of-plane and constant on concentric annuli (blue line is z-component), while at the ring-shaped domain walls between these annuli there is in-plane winding of the magnetization (orange line is the in-plane component).

For the sake of completeness, we remind that the general texture profile is $\{n_x, n_y, n_z\} \equiv \{\sin(f(r))\cos(q\theta), \sin(f(r))\sin(q\theta), \cos(f(r))\}$, with r the radial coordinate and θ the polar angle, and the explicit profile for the bubble we choose as:

$$f(r) = \pi \sum_i g(r - r_0 - r_i, w) \tag{8}$$

where $g(x, w) = (1 + \exp(-x/w))^{-1}$ is an inverted Fermi function ($g(x, w) = n_F(-x, w)$), the $r_0 = 4w$ is a global offset, and $r_i = i(L - pw/2)/p$ is the position of the i^{th} domain wall, while w is the radial width of the domain-wall.

We show in Supplementary Figure 10 the result of our radial tight-binding computations with the bubble profile of Supplementary Figure 9c. The momentum-resolved excitation spectrum, Supplementary Figure 10a, shows that the nearly-flat band and the effective gap survive; the wavefunction amplitude of the zero-energy mode (its partner is not shown) at angular momentum zero shows that the Majorana wavefunctions at the center and at the edge remain localized, although their detailed spatial profile has changed significantly.

In conclusion, if the bubbles uniform magnetization domains are not too large in real space (the radial width of the domains in above calculation is 100 sites, corresponding to a lengthscale of nm to 10 nm), our results are robust. If the domains increase, one expects to reach a regime where the ferromagnetic nature of the domains dominates, and the effective gap closes. In magnetic bubble material, the size w of a domain wall is estimated as $w = \sqrt{A/K}$ where A is the micromagnetic exchange constant and K the (effective) magnetocrystalline anisotropy Supplementary Reference 5. With the typical values $A \sim$ pJ.m^{-2} and $K \sim$ MJ.m^{-3} Supplementary Reference 5 and Supplementary Reference 6, we get $w \sim 1 - 10\,\mathrm{nm}$ which is consistent with our previous estimations for the radial winding number $p \lesssim 10$ and the skyrmion radius $R_{\mathrm{sk}} \sim 10 - 100\,\mathrm{nm}$.

Supplementary References

[1] Yang, G., Stano, P., Klinovaja, J. & Loss, D. Majorana bound states in magnetic skyrmions. *Phys. Rev. B* **93**, 224505 (2016).

[2] Kiselev, N. S., Bogdanov, A. N., Schäfer, R. & Rößler, U. K. Chiral skyrmions in thin magnetic films: new objects for magnetic storage technologies? *Journal of Physics D: Applied Physics* **44**, 392001 (2011).

[3] Makhfudz, I., Krüger, B. & Tchernyshyov, O. Inertia and chiral edge modes of a skyrmion magnetic bubble. *Phys. Rev. Lett.* **109**, 217201 (2012).

[4] Büttner, F., Lemesh, I. & Beach, G. S. D. Theory of isolated magnetic skyrmions: From fundamentals to room temperature applications. *Scientific Reports* **8**, 4464 (2018).

[5] Bernand-Mantel, A. *et al.* The skyrmion-bubble transition in a ferromagnetic thin film. *SciPost Phys.* **4**, 27 (2018).

[6] Cortés-Ortuño, D. *et al.* Nanoscale magnetic skyrmions and target states in confined geometries. *Phys. Rev. B* **99**, 214408 (2019).